PHILOSOPHICAL TRANSACTIONS A

royalsocietypublishing.org/journal/rsta

Research

Cite this article: Parto M, Sarabadani Tafreshi S, De Leeuw NH. 2026 Two-dimensional Sc_2N MXenes as efficient solid catalysts for CO_2 adsorption and conversion: a density functional theory study. *Phil. Trans. R. Soc. A* **384**: 20240472.
https://doi.org/10.1098/rsta.2024.0472

Received: 11 May 2025
Accepted: 16 August 2025

One contribution of 14 to a theme issue 'Surfaces, interfaces and heterogeneous catalysis'.

Subject Areas:
computational chemistry, energy, materials science

Keywords:
MXenes, catalysis, density functional theory, CO_2 hydrogenation

Author for correspondence:
Nora H. De Leeuw
e-mail: n.h.deleeuw@leeds.ac.uk

Electronic supplementary material is available online at https://doi.org/10.6084/m9.figshare.c.8331837.

THE ROYAL SOCIETY PUBLISHING

Two-dimensional Sc_2N MXenes as efficient solid catalysts for CO_2 adsorption and conversion: a density functional theory study

Masoumeh Parto[1], Saeedeh Sarabadani Tafreshi[1] and Nora H. De Leeuw[2,3]

[1]Department of Chemistry, Amirkabir University of Technology, Tehran, Iran
[2]School of Chemistry, University of Leeds, Leeds, UK
[3]Department of Earth Sciences, Utrecht University, Utrecht, The Netherlands

NHDL, 0000-0002-8271-0545

We have employed density functional theory (DFT) calculations to explore the catalytic potential of scandium nitride (Sc_2N) MXenes for CO_2 capture and hydrogenation to methane. The Sc_2N surface exhibits a strong affinity for CO_2 with an adsorption energy of –3.627 eV, surpassing values reported for other MXenes, such as Ti_2N and V_2N, and even outperforming conventional catalysts like Pt(111). Charge density difference and COHP analyses reveal significant back-donation from Sc d-orbitals to the antibonding orbitals of CO_2, resulting in the formation of activated $CO_2^{\delta-}$ species. AIMD simulations confirm the thermal stability of Sc_2N under ambient conditions. The hydrogenation pathway to CH_4 proceeds via eight elementary steps, with the $CH_2OH + H \rightarrow CH_3OH$ reaction identified as the rate-determining step due to its high activation barrier (2.916 eV). Sc_2N effectively stabilizes key intermediates, such as COOH, HCOOH and CH_2OH, and facilitates H_2 dissociation with moderate energy requirements. Compared with other MXenes, Sc_2N shows superior ability to stabilize intermediates, particularly HCOOH, which plays a crucial role in the conversion pathway. However, large negative adsorption energies for H and O atoms suggest potential surface poisoning, which may limit

catalytic turnover unless regeneration strategies are implemented. These findings highlight Sc_2N MXenes as robust and efficient materials for CO_2 capture and conversion, although further optimization is necessary for sustained catalytic performance.

This article is part of the theme issue 'Surfaces, interfaces and heterogeneous catalysis'.

1. Introduction

Since the onset of the second industrial revolution [1], characterized by increasing automation and mass production, the global production of various entities, e.g. cement, electricity, energy and goods for household consumption, has relied heavily on the combustion of fossil fuels [2]. However, this practice has resulted in the substantial release of carbon dioxide (CO_2) into the Earth's atmosphere [3], with global carbon dioxide emissions surging by more than 70% between 1970 and 2002 [4]. Unfortunately, this anthropogenic production of CO_2 is no longer balanced by natural capture, conversion and storage. CO_2 is a potent greenhouse gas [5] that contributes to the rise in the Earth's temperature through the trapping and re-emission of infrared radiation [6,7]. The consequences of global warming are far-reaching and include phenomena such as floods, droughts and the extinction of plant and animal species [8]. In view of this harmful climate change, the capture and transformation of CO_2 into benign or even beneficial products have become paramount.

Carbon dioxide is a linear and remarkably stable molecule, featuring carbon in its highest oxidation state, and the C = O bond within CO_2 is thermodynamically stable [9]. Disrupting this bond and activating carbon dioxide for further reactions requires a substantial amount of energy and high temperatures [9]. Furthermore, the chemical stability of carbon dioxide underscores its weak interaction with solid surfaces. Effective CO_2 adsorption typically occurs at elevated temperatures and under significant partial pressures, often involving charge transfer processes that result in the creation of bent, anionic CO_2 species ($CO_2^{\delta-}$) [10]. The use of solid catalysts has garnered significant attention in this process, owing to their non-corrosive nature, cost-effectiveness and ease of regeneration, making them advantageous for CO_2 capture and conversion [11,12], which is the basis for many of the approaches suggested for carbon capture and utilization (CCU) strategies to mitigate CO_2 emissions [13].

Recent years have witnessed the development of two-dimensional materials with exceptional properties, including extraordinarily high specific surface areas with substantial proportions of exposed surface atoms, rendering them promising candidates for CO_2 adsorption and reduction. Among these materials, MXenes have emerged as a notable group. MXenes are derived from transition metal carbides and nitrides and are obtained from MAX phases with the formula $M_{n+1}AX_n$, where M represents the transition metal, A is an element from group 13 or 14 of the periodic table, X is either carbon or nitrogen, and the value of n, which ranges from 1 to 3, determines the atomic layers of the resulting material, ranging from 3 or 5 to 7 layers [14]. The two-dimensional structure of MXenes, facilitated by the presence of vacant d-orbitals of the metals in their surfaces, enables efficient gas adsorption [15]. In a groundbreaking development in 2011, MXenes were first synthesized through the production of Ti_3C_2 during an etching process, accomplished by dissolving Ti_3AlC_2 in hydrofluoric acid (HF; [16]). Most MXenes are synthesized through a three-layer hexagonal etching process of the MAX phase using various acids, effectively removing layer A from the structure and yielding two-dimensional MXenes [17,18]. For example, Sc_2N MXene can be produced from the Sc_2AlN MAX phase by removing the aluminium (Al) layer through chemical etching, using acids like HF, or through molten salt processes [19,20]. After etching, the resulting two-dimensional structure consists of a hexagonal arrangement of scandium and nitrogen atoms, with exposed active sites that can interact with gas molecules such as CO_2.

Notably, the substantial adsorption energy released by carbon dioxide binding to M_2N surfaces compared with similar carbides (M_2C) positions M_2N materials as the more suitable candidates for CO_2 activation and conversion, which show enhanced CO_2 adsorption and catalytic properties owing to their electron-rich nitrogen layers [10].

Recent efforts have focused on tailoring MXene surfaces through functionalization or heterostructure design to improve catalytic selectivity and reduce energy barriers for CO_2 hydrogenation [21]. Moreover, very recent studies have demonstrated that tuning the electronic properties of MXene materials via compositional engineering or metal–support interactions can yield promising results in terms of both adsorption capacity and catalytic turnover for CO_2 reduction to CH_4 and other value-added products [22,23].

Scandium nitride (Sc_2N) MXenes, in particular, present a promising material for catalytic applications. First-principles calculations have predicted the thermodynamic stability, structural robustness and metallic conductivity of Sc-based MXenes, highlighting their potential as a promising two-dimensional catalyst [24]. Further studies have examined the influence of surface terminations, magnetism and charge transport in Sc-based MXenes [19,25]. The unique structural features of MXenes, including their tuneable surface chemistry and electronic properties, have been studied extensively by researchers, who have highlighted the role of surface terminations (e.g. -O, -OH and -F groups) in modulating the adsorption properties of MXenes. Such surface modifications can further enhance the catalytic performance of Sc_2N by tailoring its electronic structure to facilitate CO_2 reduction [26]. Recent work also points to the high carrier mobility and low work function of Sc_2N, which are favourable for electronic and catalytic applications [24,26]. In addition, related scandium-based MXenes, such as Sc_2C, have been investigated for thermoelectric applications, where surface functionalization was shown to enhance the Seebeck coefficient and improve overall energy conversion performance [27]. Furthermore, doped Sc-based MXenes have recently been predicted to exhibit s–p–d band inversion, identifying them as a new class of topological insulators with potential relevance for quantum and spintronic devices [28].

Recent experimental work has demonstrated that two-dimensional functionalized Sc-based MXenes synthesized via sputtering exhibit semiconductive behaviour with strong optical absorption in the visible region, suggesting their potential for optoelectronic and photocatalytic applications [29]. Moreover, Sc_2N has been highlighted in computational screening studies of MXenes for H_2 adsorption and dissociation, where its electron-rich nitrogen layers promote strong binding with molecules [30]. Although there have only been limited studies on Sc_2N, theoretical research indicates that it exhibits stronger CO_2 adsorption energies compared with other MXenes, e.g. Ti_2N and Zr_2N [31].

In this context, our study employs calculations based on the density functional theory (DFT) to investigate the CO_2 adsorption and hydrogenation behaviour on Sc_2N monolayers, evaluating its capacity to catalytically convert CO_2 to methane. The findings are discussed in relation to prior theoretical insights into Sc_2N and broader MXene-based CO_2 reduction mechanisms.

2. Computational models and methods

In this work, we have constructed the monolayer structure of Sc_2N MXene based on crystallographic data, before performing full geometry optimization using DFT calculations. The optimized structure is shown in figure 1 and consists of a hexagonal arrangement of scandium and nitrogen atoms in a layered configuration. A triclinic unit cell, with lattice constants of a = 12.685 Å, b = 12.685 Å and c = 14.408 Å, was optimized to achieve a stable surface configuration. The sandwich-like arrangement of scandium atoms on both sides of the nitrogen layer offers enhanced surface reactivity, similar to what has been observed in Ti_2N and Nb_2N MXenes [25].

The electronic structures and catalytic properties of Sc_2N MXenes were investigated via DFT [32,33] calculations using the Vienna Ab initio Simulation Package (VASP) [34–36]. The generalized gradient approximation [37] was applied with the Perdew–Burke–Ernzerhof

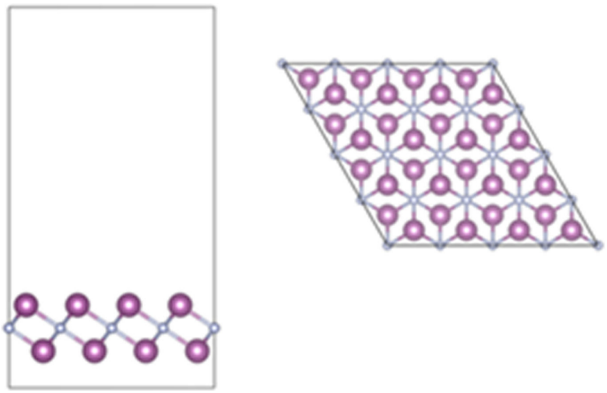

Figure 1. Side and top views of the optimized Sc_2N MXene structure used in the DFT calculations (Sc = purple, N = blue). The structure features a layered hexagonal configuration with exposed scandium atoms in both surfaces.

functional [38], which has been used widely in studies of CO_2 adsorption at various MXenes [39]. The interaction between the valence electron density and the core electrons is described using the projector augmented wave method [40]. Similar computational frameworks have been employed in other studies on CO_2 adsorption at metal oxides and MOFs, where DFT simulations have provided critical insights into interaction mechanisms at the atomic level [41,42].

A plane-wave cut-off energy of 800 eV was used, which was determined through convergence tests, as shown in the electronic supplementary material, figure 1Sa. The choice of this energy cut-off is critical to ensure the convergence of the results. Previous research on Ti_3C_2 and Nb_2N MXenes has demonstrated that cut-off energies in the range of 500–800 eV are sufficient to ensure accurate simulation results at an acceptable computational cost [43]. Monkhorst–Pack *k*-point grids of 5 × 5 × 1 and 11 × 11 × 1 were employed to sample the Brillouin zone, ensuring high precision in the calculation of adsorption energies and electronic interactions [44], respectively, as illustrated in electronic supplementary material, figure 1Sb.

Long-range dispersion interactions were accounted for using the Grimme D3 correction scheme, which was included in all calculations to improve the accuracy of adsorption energies and weak intermolecular interactions, consistent with previous studies on catalytic systems [45–47].

The CO_2 adsorption process on the Sc_2N surface was modelled by placing a CO_2 molecule at various potential adsorption sites, including the top, bridge and hollow sites. The adsorption energy for each molecule at the surface was then calculated using the following formula:

$$E_{ads} = E_{A+slab} - E_{slab} - E_A\,. \tag{2.1}$$

In this equation, E_{ads} represents the adsorption energy, E_{A+slab} corresponds to the energy of the system of an adsorbed molecule on the catalyst surface and E_A and E_{slab} denote the energies of the isolated molecule in vacuum and the energy of the pristine surface, respectively. A large negative E_{ads} value indicates a stable configuration and exothermic adsorption [48].

To simulate the hydrogenation of each adsorbed CO_2, COOH, HCOOH, HCO, H_2CO, CH_2OH, CH_3OH and CH_3 molecule, a hydrogen atom must be positioned appropriately according to the expected product of the hydrogenation reaction. In this regard, nine reactions were investigated from a selected pathway, comprising molecules and hydrogen gas as the initial state and progressing to the respective products. The reaction energy for each step was calculated using the following equation:

$$E_{reac} = E_f - E_{in}\,, \tag{2.2}$$

where E_f represents the energy of the final state and E_{in} represents the energy of the initial state.

The nudged elastic band [49,50] method was employed to determine the reaction path and transition state between the reactant and product states. Intermediate states are identified, and the activation energy for each reaction is calculated using the following equation:

$$E_a = E_{TS} - E_{in}, \tag{2.3}$$

where E_a represents the activation energy, E_{TS} is the energy of the intermediate state of the reaction and E_{in} is the energy of the initial state in each reaction.

To assess the thermodynamic stability of the Sc_2N catalyst, we performed *ab initio* molecular dynamics (AIMD) simulations using the Nosé–Hoover thermostat in the NVT ensemble at 300 K for 20 ps with a time step of 1 fs as implemented in the VASP package. The structural integrity of the Sc_2N surface was monitored throughout the trajectory, and the temperature and energy fluctuations were analysed to confirm stability.

3. Results and discussion

The optimized structure of the Sc_2N MXene revealed a highly stable configuration, with minimal distortion during surface relaxation. This stability is essential in maintaining catalytic activity during reaction cycles, as structural degradation can lead to deactivation of the catalyst [51]. Similar surface stability has been observed in other MXenes, e.g. Ti_2N and Zr_2N [52]. To demonstrate the thermal stability of the catalyst, AIMD simulations were performed for the Sc_2N monolayer at 300 K. The results reveal that the structure remains stable over the entire 20 ps simulation, with no evidence of bond breaking, surface reconstruction or significant distortion. As illustrated in figure 2, the total energy fluctuates within a narrow range, while the system temperature remains consistently close to the target value, indicating effective thermal regulation by the Nosé–Hoover thermostat. Representative snapshots of the initial and final configurations (figure 2) confirm the preservation of the surface morphology. These findings provide strong evidence of the thermodynamic robustness of Sc_2N under ambient conditions, underscoring its suitability for practical catalytic applications.

The CO_2 reduction process focused on in this work involves eight elementary steps [53], which can be represented as a pathway starting from CO_2 and proceeding through seven surface-bound intermediates as follows:

$$CO_2 \rightarrow COOH \rightarrow HCOOH \rightarrow HCO \rightarrow H_2CO \rightarrow CH_2OH \rightarrow CH_3OH \rightarrow CH_3 \rightarrow CH_4$$

The intermediates were simulated and adsorbed at the Sc_2N surface in different positions, with the optimal position for each molecule determined through geometry optimizations.

(a) Sc_2N electronic properties

The electronic structure of the Sc_2N monolayer was elucidated through projected density of states (PDOS) analysis, as shown in figure 3. The total density of states (TDOS) exhibits a prominent peak at the Fermi level (set to 0 eV), which clearly indicates the metallic nature of Sc_2N. The absence of a band gap further supports its intrinsic metallicity, consistent with prior predictions for early transition metal-based MXenes [24]. The PDOS reveals that the states near the Fermi level are primarily derived from the Sc 3d-orbitals, while N 2p-orbitals mainly contribute to deeper valence states in the range of −6 to −3 eV. This orbital distribution suggests significant Sc–N hybridization, contributing to the structural stability and electronic delocalization.

Moreover, the strong presence of unoccupied Sc d-states above the Fermi level implies high electronic activity, which can be beneficial for catalytic applications, such as hydrogen evolution

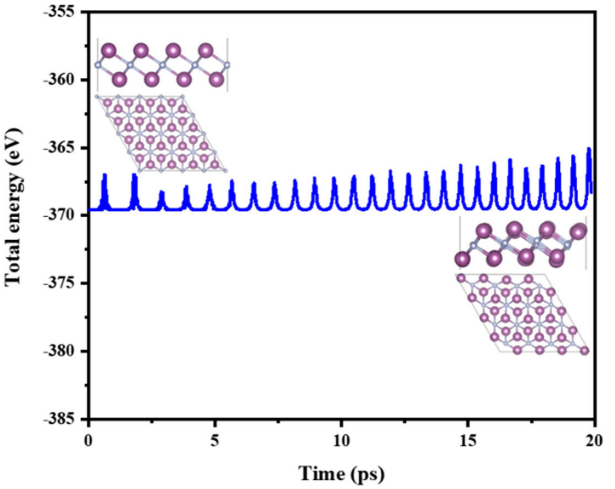

Figure 2. Time evolution of total energy of the Sc_2N surface during a 20 ps AIMD simulation at 300 K, also showing snapshots of the Sc_2N surface at the start and end of the 20 ps AIMD simulation at 300 K.

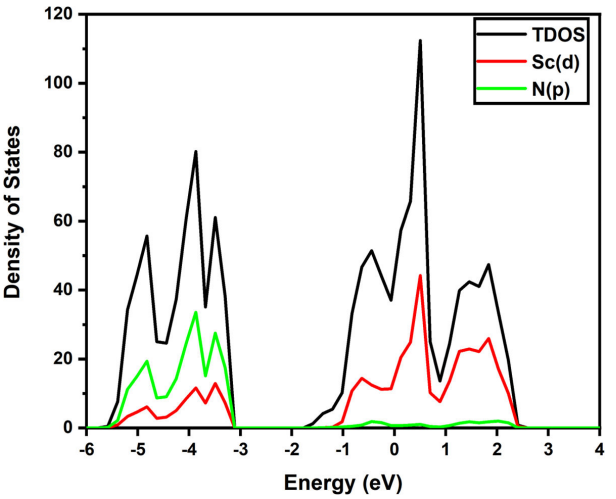

Figure 3. Orbital-projected density of states (PDOS) for the Sc_2N monolayer. The total density of states (TDOS.) is shown in black, while the contributions from Sc 3d- and N 2p-orbitals are shown in red and green, respectively. The Fermi level is set to 0 eV.

or CO_2 reduction reactions. Similar behaviour has been reported in Ti_2N and V_2C MXenes, where conduction bands dominated by d-orbitals promote metallic conductivity and enhance surface reactivity [16].

(b) CO_2 adsorption

One of the primary challenges in developing a heterogeneous catalyst for CO_2 adsorption, activation and reduction is establishing a robust interaction between CO_2 and the solid surface. The adsorption of CO_2 on the Sc_2N surface was found to be highly favourable, with an adsorption energy of −3.627 eV. This interaction is stronger than those reported for other MXenes, such as Ti_2N (−3.13 eV) and V_2N (−1.67 eV) [31]. The hollow site, where both oxygen atoms of the CO_2 molecule can interact with scandium atoms, was determined to be the most stable adsorption configuration, as depicted in figure 4, which is consistent with findings from

previous studies on CO_2 adsorption at transition metal carbides and nitrides, where hollow sites often provide the most favourable binding energies [54]. In comparison, platinum-based catalysts, which are commonly used for CO_2 electro-reduction, do not adsorb CO_2 (adsorption energy of +0.51 eV), highlighting the superior CO_2 binding capacity of Sc_2N [55]. The strong interaction between CO_2 and the Sc_2N surface can be attributed to the electron-donating capability of the scandium d-orbitals, which facilitate back-donation to the CO_2 molecule, thereby enhancing adsorption and activating the CO_2 molecule ready for reduction [31,56,57]. To quantify this interaction, we have performed a Bader charge analysis [58], which reveals a charge transfer of $1.746e^-$ from the Sc_2N surface to the CO_2 molecule. This substantial electron transfer suggests the formation of a $CO_2^{\delta-}$ species, a key indicator of activation. Furthermore, the charge density difference plot shown in figure 5 highlights charge accumulation around the CO_2 oxygen atoms and corresponding depletion around scandium atoms, consistent with d-orbital-mediated back-donation and confirming strong electronic coupling between the surface and the adsorbate. The charge density difference was calculated as $\Delta\varrho = \varrho(CO_2/Sc_2N) - \varrho(Sc_2N) - \varrho(CO_2)$, where $\varrho(CO_2/Sc_2N)$ is the charge density of the adsorbed system, $\varrho(Sc_2N)$ is the charge density of the clean surface and $\varrho(CO_2)$ is the charge density of the isolated CO_2 molecule in the same configuration.

To further explore the nature of the CO_2–Sc_2N interaction, we have also performed orbital-PDOS analysis (figure 6). The PDOS reveals pronounced overlap between the O 2p-orbitals of CO_2 and the Sc 3d-orbitals of the substrate around the Fermi level. This interaction is indicative of orbital hybridization and supports the presence of electron back-donation from Sc_2N to the antibonding orbitals of CO_2, facilitating its activation. These results are consistent with previous studies on MXene–CO_2 systems, where similar orbital interactions have been linked to strong chemisorption and efficient charge transfer [59,60].

To further investigate the bonding nature and interaction mechanism between CO_2 and the Sc_2N surface and to elucidate the bonding characteristics between key atom pairs, namely C–O and Sc–O, we have performed a crystal orbital Hamilton population (COHP) analysis using the LOBSTER code [61–64], as shown in figure 7a. The structural model identifying the specific C–O and Sc–O bonds under analysis is shown in figure 7b. The two internal C–O bonds of the CO_2 molecule (C–O (1) and C–O (2)) exhibit strong bonding character, as indicated by the significant negative peaks in the pCOHP plots below the Fermi level. These states extend from approximately –10 eV up to –3 eV, and the corresponding integrated COHP (ICOHP) values are –10.65 eV and –10.68 eV, confirming their robust covalent nature.

In contrast, the four Sc–O bonds that anchor the CO_2 molecule to the Sc_2N surface show moderate bonding interactions, with ICOHP values ranging from –1.65 eV to –1.96 eV. The pCOHP curves for these bonds show modest bonding contributions below the Fermi level (–10 to –2 eV) and some antibonding states just above it (positive values), reflecting the partial covalent character of the Sc–O interactions. These antibonding features indicate back-donation from Sc d-orbitals to CO_2 antibonding orbitals, which contributes to CO_2 activation. Overall, the COHP analysis supports the conclusion that the Sc_2N surface effectively activates CO_2 via moderate Sc–O interactions, while preserving the internal bonding structure of CO_2.

(c) H_2 dissociation

Efficient activation and dissociation of hydrogen molecules (H_2) are a crucial step in catalytic hydrogenation, particularly in the CO_2 conversion reactions studied here. To assess the hydrogen activation capability of Sc_2N MXene, we have investigated the dissociative adsorption of H_2, shown in figure 8.

The dissociation of H_2 on the Sc_2N surface was modelled as a surface reaction from molecular adsorption to two adsorbed H atoms:

$$H_{2(ads)} \rightarrow 2H_{(ads)}$$

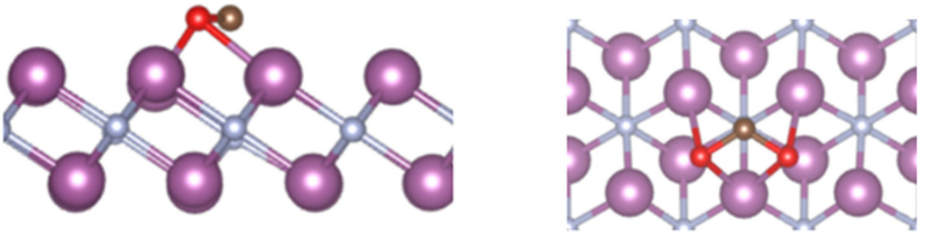

Figure 4. Side and top views of the adsorbed CO_2 molecule in the hollow position of the Sc_2N surface (Sc = purple, N = blue, O = red, C = brown).

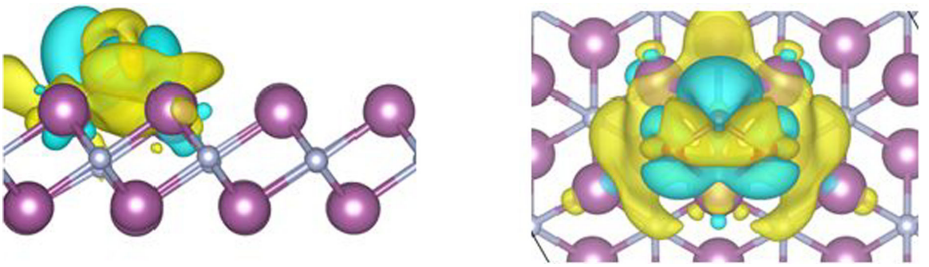

Figure 5. Side and top views of the charge density difference plot for CO_2 adsorption on the Sc_2N surface. Yellow and blue isosurfaces represent regions of charge depletion and accumulation, respectively (isosurface value = ± 0.002 e^- $Å^{-3}$).

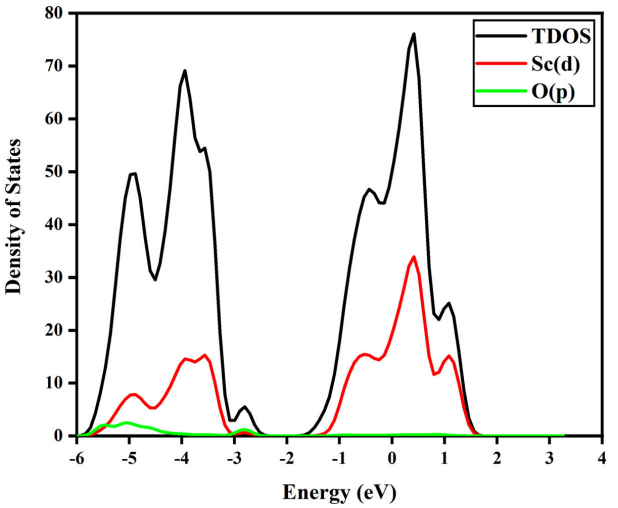

Figure 6. Orbital-projected density of states (PDOS) for the CO_2–Sc_2N system. The total density of states (TDOS) is shown in black, while the contributions from Sc 3d-orbitals of Sc_2N and O 2p-orbitals of CO_2 are shown in red and green, respectively. The Fermi level is set to 0 eV.

The corresponding dissociation energy was calculated as the total energy difference between these two adsorbed states:

$$E_{\text{diss}} = E_{2\text{H}/\text{Sc}_2\text{N}} - E_{\text{H}_2/\text{Sc}_2\text{N}},$$

where $E_{2\text{H}/\text{Sc}_2\text{N}}$ and $E_{\text{H}_2/\text{Sc}_2\text{N}}$ are the total energies of the Sc_2N surface with two individual hydrogen atoms and a molecular H_2 adsorbed on the surface, respectively.

Our results indicate that H_2 dissociation at the Sc_2N surface is thermodynamically favourable, with a reaction energy of –1.71 eV and an activation energy of 0.75 eV. While this represents

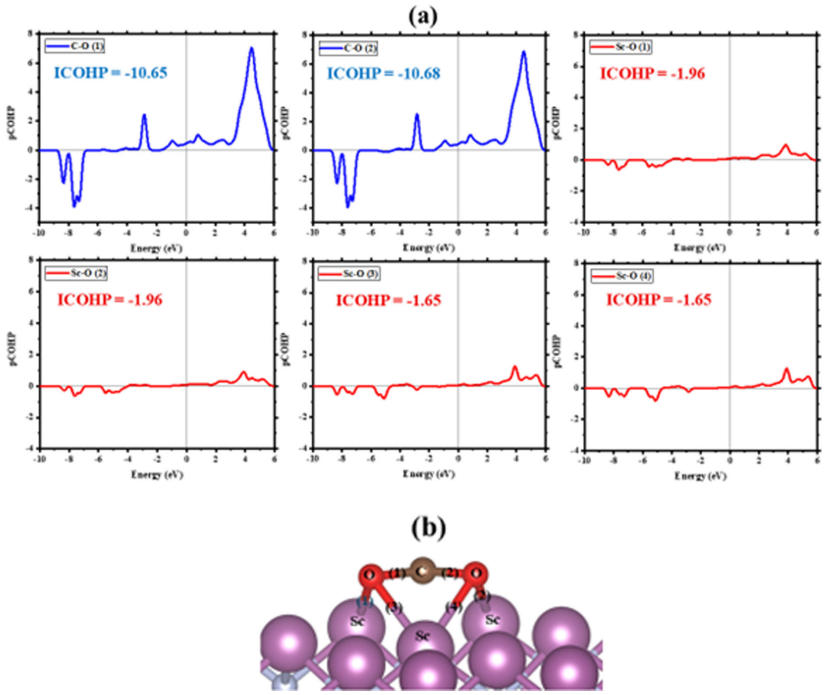

Figure 7. (a) Projected crystal orbital Hamilton population (pCOHP) curves for the labelled atom pairs involved in the adsorption of a CO_2 molecule on the Sc_2N surface. Curves are aligned to the Fermi level ($E = 0$ eV). (b) Atomic structure and bond labelling for CO_2 adsorbed on the Sc_2N monolayer. The numbered bonds correspond to those analysed in the pCOHP plots shown in (a), with C–O bonds labelled as (1) and (2), and Sc–O bonds labelled as (1) to (4).

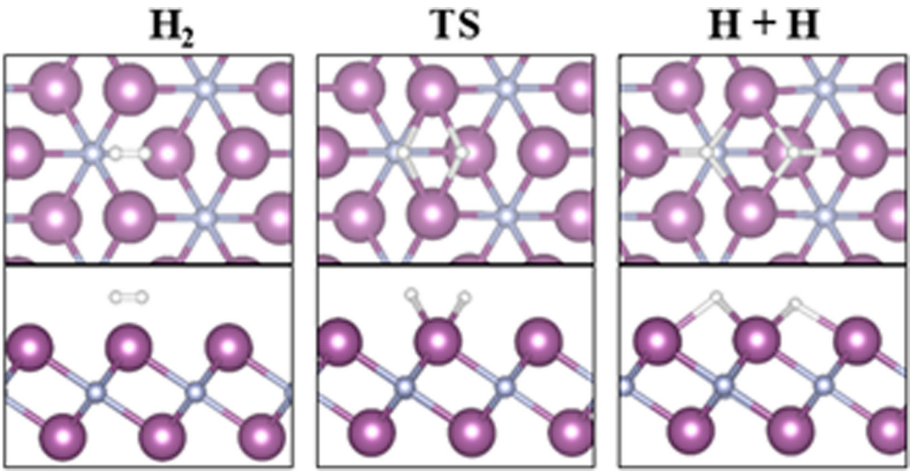

Figure 8. Top and side views of optimized geometries for H_2 molecular adsorption (left) and dissociative H adsorption (right) on the Sc_2N surface. (Sc = purple, N = blue, H = white).

a moderate energy barrier, it suggests that the reaction is kinetically feasible but would require energy input to proceed at a significant rate under ambient conditions. After dissociation, each hydrogen atom binds strongly to adjacent scandium sites, stabilized through the formation of Sc–H bonds. The high reactivity of Sc_2N can be attributed to the metallic character of the surface and the presence of exposed Sc atoms, which promote electron transfer into the antibonding σ^* orbital of H_2, thereby facilitating bond breaking. Such behaviour is consistent with trends

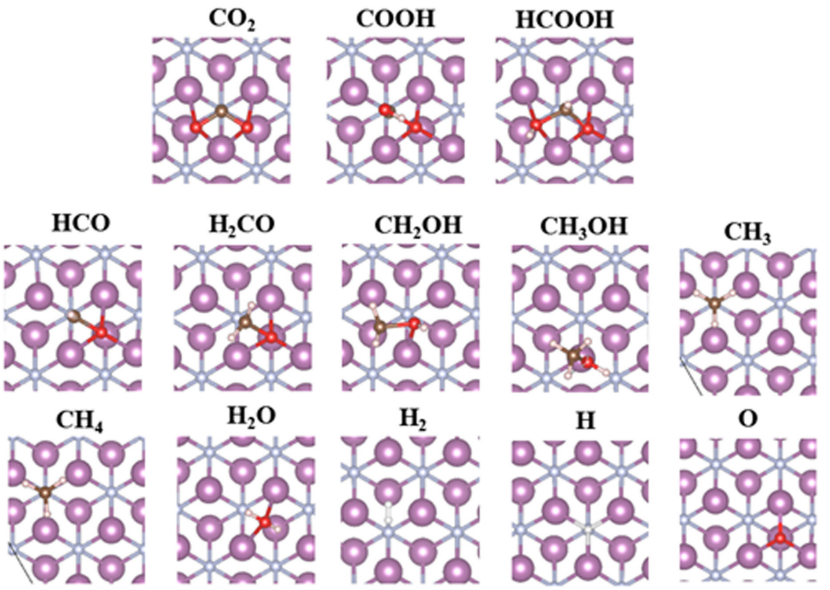

Figure 9. Top view of the lowest energy adsorption structures of CO_2, COOH, HCOOH, HCO, H_2CO, CH_2OH, CH_3OH, CH_3, CH_4, H_2O and H_2 molecules and H and O atoms on the Sc_2N surface (Sc = purple, N = blue, O = red, C = brown, H = white).

Table 1. Adsorption geometries and energies of key intermediates on the Sc_2N surface, compared with selected values from other catalysts. The adsorption energies of H and O atoms were calculated using one-half $E(H_2)$ and one-half $E(O_2)$ as reference states, respectively, to ensure consistency with standard DFT methodology [30].

intermediate	site, atom, bond length (Å)	E_{ads} (eV) on Sc_2N	E_{ads} (eV) on Ti_2N [65]	E_{ads} (eV) on Pt(111) [66,67]
CO_2	hollow, oxygen, 2.420	−3.627	−3.13	−2.78
COOH	hollow, oxygen, 2.420	−5.184	−4.61	−4.32
HCOOH	hollow, oxygen, 2.420	−3.659	−3.299	−3.05
HCO	hollow, oxygen, 2.420	−5.728	−4.639	−5.94
H_2CO	hollow, oxygen, 2.420	−4.067	—	—
CH_2OH	hollow, oxygen, 2.420	−3.851	−3.18	−3.50
CH_3OH	top, oxygen, 2.420	−2.673	—	—
CH_3	hollow, carbon, 2.486	−3.562	−4.50	−4.00
CH_4	hollow, carbon, physical adsorption	−0.103	−2.93	−2.45
H_2O	hollow, oxygen, 2.420	−1.127	—	—
H_2	hollow, hydrogen, 2.135	−0.225	—	—
H	hollow, hydrogen, 2.076	−1.067	—	−2.71
O	hollow, hydrogen, 2.029	−5.744	—	−3.74

reported for early transition metal surfaces and MXenes, where low-coordinated metal sites lower the barrier for H_2 activation [30].

Compared with previously studied MXenes and transition metal carbides/nitrides, where H_2 dissociation is moderately exothermic [30], the dissociation energy on Sc_2N (−1.71 eV) indicates a particularly strong interaction, highlighting the excellent ability of Sc_2N towards H_2 activation.

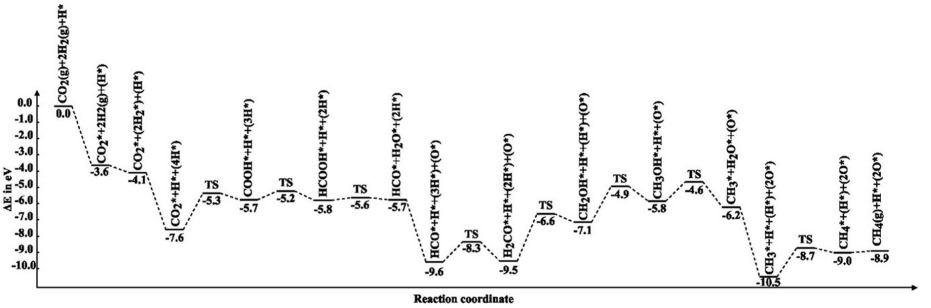

Figure 10. Reaction profile illustrating the hydrogenation of CO_2 and its intermediates to CH_4 on the Sc_2N surface. Atoms in parentheses are included to maintain atomic balance.

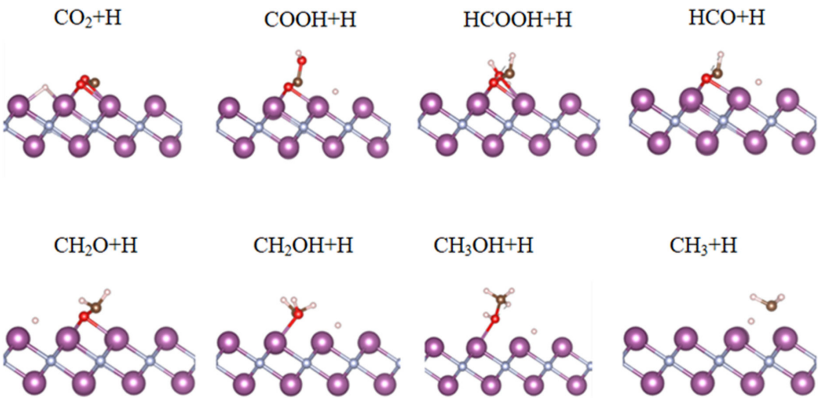

Figure 11. Adsorption of a hydrogen atom next to the target molecules CO_2, COOH, HCOOH, HCO, H_2CO, CH_2OH, CH_3OH and CH_3 (Sc = purple, N = blue, O = red, C = brown, H = white).

The facile H_2 dissociation on Sc_2N, combined with its strong CO_2 adsorption capacity (discussed in §3b), positions Sc_2N as a promising dual-activation platform, capable of simultaneously activating hydrogen and carbon dioxide, which is essential for efficient catalytic hydrogenation pathways towards methanol or methane.

(d) Adsorption energies and stabilities of intermediates

The adsorption energies of key intermediates, including the CO_2, COOH, HCOOH, HCO, H_2CO, CH_2OH, CH_3OH, CH_3, CH_4, H_2 and H_2O molecules and H atoms, were found to be highly favourable, indicating strong binding with the Sc_2N surface (see table 1). This strong interaction is crucial to stabilize reaction intermediates during the CO_2 conversion process, which directly impacts the selectivity and efficiency of the catalyst. The optimal adsorbed geometries, characterized by the largest adsorption energies, are shown in figure 9.

The large adsorption energies indicate that Sc_2N offers a more stable platform for CO_2 reduction compared with other MXenes and traditional catalysts like Pt and Pd. For instance, the adsorption energy for HCOOH on Sc_2N (−3.659 eV) is notably higher than that on Ti_2N (−3.299 eV), suggesting that Sc_2N is more effective at stabilizing this intermediate, which is a crucial step in the methane production pathway [65].

The stability of other intermediates at the Sc_2N surface is comparable to observations for transition metal oxides. In other studies, it has been shown that metal oxide surfaces with appropriate terminations can stabilize reaction intermediates, leading to improved catalytic activity for CO_2 reduction [68]. The strong adsorption energies observed for intermediates like

COOH and CH_2OH on Sc_2N suggest that this MXene may function similarly to modified metal oxides, providing enhanced stability in key reaction steps [69].

(e) CO_2 hydrogenation pathway and activation energies

During CO_2 reduction, various carbon-based products can be generated, including carbon monoxide (CO), formic acid (HCOOH), formaldehyde (HCHO), methanol (CH_3OH), ethylene (C_2H_4) and methane (CH_4). In this study, we were particularly interested in the pathway to methane through CO_2 hydrogenation, via a number of partially hydrogenated intermediates. Multiple mechanisms have been proposed for CH_4 production through CO_2 reduction. Here, we have focused exclusively on the CO_2 hydrogenation pathway that proceeds via the formation of formic acid (HCOOH). This pathway was selected based on previous theoretical studies indicating that the COOH → HCOOH conversion plays a central role in determining the efficiency of CO_2 reduction over transition metal and MXene surfaces [21,46,47,66]. Accordingly, our investigation starts with the COOH intermediate and follows sequential hydrogenation steps through HCOOH, HCO, and beyond: CO_2 → COOH → HCOOH → HCO → H_2CO → CH_2OH → $HOCH_3$ → CH_3 → CH_4, as shown in figure 10. The adsorption energies of COOH and HCOOH on the Sc_2N surface were calculated to be −5.184 and −3.659 eV, indicating very strong interactions, which stabilize the intermediates and facilitate further reduction.

The CO_2 reduction pathway selected for this study comprises eight steps, with each step involving the adsorption of a hydrogen atom next to the target molecule, i.e. CO_2, COOH, HCOOH, CHO, H_2CO, CH_2OH, CH_3OH and CH_3, as illustrated in figure 11. The reaction energies calculated via equation (2.2) are presented in table 2. To determine the rate-determining step characterized by the highest activation energy, we employed equation (2.3) to calculate the activation energy for each reaction, as listed in table 2. Each elementary step in this pathway, shown in figure 12, has been analysed and compared with results from similar studies on MXenes and other catalytic surfaces, as described below.

CO_2 + H → COOH: The first reaction step, converting CO_2 to COOH, is highly endothermic (1.553 eV) and requires a considerable activation energy (2.222 eV), indicating that it is an energy-intensive initiation process. Previous studies have also suggested that activating CO_2 on MXene surfaces like Sc_2N requires significant activation energies to be overcome, although these can be reduced with suitable surface functionalization [31,70]. In comparison with Ti_3C_2 and other MXenes, where activation energies for CO_2 to COOH conversion have been recorded at 1.8–2.0 eV, the process on Sc_2N requires a little more energy, suggesting that this potential catalyst could benefit from structural modifications [71,72].

COOH + H → HCOOH: The second reaction step, reducing COOH to HCOOH, is exothermic with a reaction energy of −0.205 eV and a low activation energy of 0.550 eV, suggesting a more favourable energy profile. In other MXene studies, e.g. those involving Ti_2C and Mo_2TiC_2, activation energies ranged between 0.4 and 0.6 eV for this step, i.e. very similar to Sc_2N [73,74]. This alignment highlights that Sc_2N MXene could achieve similar catalytic performance to other MXenes, particularly in formic acid production, where low activation barriers are advantageous for efficient reduction.

HCOOH + H → HCO + H_2O: The third step, converting HCOOH to HCO and H_2O, has an almost zero reaction energy (0.010 eV) and an activation energy of only 0.152 eV, indicating that this step proceeds readily. Similar low-barrier pathways were observed in studies of metal oxide-supported MXenes, where the activation energies were comparably low. For instance, Mo_2TiC_2 MXene on TiO_2 shows similarly low energy demands, supporting the suggestion that MXenes like Sc_2N might efficiently facilitate this step in the reaction sequence [73].

HCO + H → H_2CO: Here, the step to form H_2CO has a moderately positive reaction energy (0.290 eV) and an activation energy of 1.246 eV, i.e. a higher energy requirement than the two previous steps, but easier to achieve than the first hydrogenation step of the CO_2 molecule.

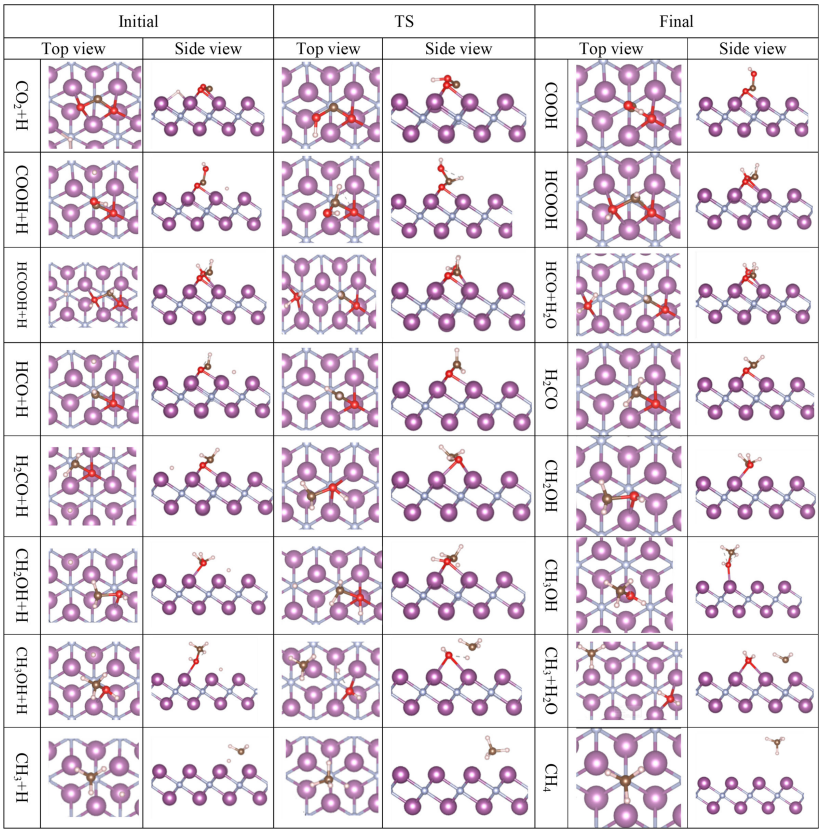

Figure 12. The selected reactions with their corresponding initial, transition (TS) and final states at the $Sc_2N(001)$ surface (Sc = purple, N = blue, O = red, C = brown, H = white).

Table 2. Calculated reaction (E_{react}) and activation (E_a) energies for all elementary hydrogenation reactions on the Sc_2N surface.

reaction	E_{react} (eV)	E_a (eV)
$CO_2 + H \rightarrow COOH$	1.553	2.222
$COOH + H \rightarrow HCOOH$	−0.205	0.550
$HCOOH + H \rightarrow HCO + H_2O$	0.01	0.152
$HCO + H \rightarrow H_2CO$	0.29	1.246
$H_2CO + H \rightarrow CH_2OH$	2.619	2.916
$CH_2OH + H \rightarrow CH_3OH$	1.709	2.185
$CH_3OH + H \rightarrow CH_3 + H_2O$	−0.378	1.192
$CH_3 + H \rightarrow CH_4$	1.481	1.761

Studies involving MXenes such as Ti_3C_2 have shown slightly lower activation energies (around 1.0–1.1 eV) for this step, indicating again that Sc_2N may benefit from additional surface optimization to match the efficiency of other MXenes in facilitating formaldehyde formation [71,72].

$H_2CO + H \rightarrow CH_2OH$: The reduction of H_2CO to CH_2OH stands out as the most energy-intensive step, with a reaction energy of 2.619 eV and an activation energy of 2.916 eV, which may limit the overall efficiency of the reaction pathway over Sc_2N. This high energy demand

is consistent with reports on other MXenes like Nb_2C, where energy requirements peak at this step, although alternative configurations on MXenes like V_2C have shown potential to reduce the energy to around 2.5 eV [46,57,75]. Despite the challenges facing the application of Sc_2N for this step, structural tuning or alloying could reduce the energy barrier and improve performance.

$CH_2OH + H \rightarrow CH_3OH$: The conversion to methanol (CH_3OH) is exothermic, with a reaction energy of −1.709 eV and an activation energy of 2.185 eV, indicative of a favourable methanol production pathway despite the high activation energy. Sc_2N compares with Ti_3C_2 and Mo_2TiC_2, where previous studies have identified similar activation energies in the range of 1.8–2.0 eV. This suggests that methanol production on Sc_2N MXene could potentially be competitive with other MXenes under optimized conditions [71,72].

$CH_3OH + H \rightarrow CH_3 + H_2O$: This exothermic step with a reaction energy of −0.378 eV and activation energy of 1.192 eV indicates that forming CH_3 and H_2O is feasible. The relatively low activation energy aligns well with findings on other MXenes like Ti_3C_2, where barriers are typically under 1.3 eV [71,72]. This similarity underscores that Sc_2N could perform effectively at this stage, aligning with other promising MXenes.

$CH_3 + H \rightarrow CH_4$: The final step in methane production shows a positive reaction energy of 1.481 eV and an activation energy of 1.761 eV, comparable to MXenes like Nb_2C and Ti_3C_2, which exhibit activation energies in the range of 1.5–1.8 eV for this step. Sc_2N falls within the expected limits, suggesting it could be similarly viable for methane synthesis in a CO_2 reduction pathway [46,71,72,75].

While the reaction energy profile (figure 10) shows a strongly downhill thermodynamic trend, this behaviour is largely influenced by the inclusion of co-adsorbed H and O species required to maintain stoichiometric balance between intermediates. This effect is due to their strong surface adsorption energies and is a standard feature in DFT-based reaction profiles that include co-adsorbed species [30]. These species bind very strongly to the Sc_2N surface, leading to substantial energy drops at key points in the reaction coordinate. Notably, the adsorption energies of H and O (–1.067 and –5.744 eV, respectively) suggest that surface regeneration may be kinetically limited under reaction conditions. Such strong adsorption could hinder the release of products and block active sites, ultimately affecting the catalytic turnover frequency. This issue has also been noted for other MXene systems, as discussed in the recent literature [39], where excessive binding strength can impair the desorption of reaction intermediates such as OH*, O* or H*, leading to potential catalyst poisoning.

4. Conclusion

This study presents a comprehensive theoretical investigation of Sc_2N MXenes as promising catalysts for CO_2 capture and conversion. AIMD simulations validate the thermal stability of Sc_2N, indicating its viability under operational temperatures.

DFT calculations demonstrate that Sc_2N has a high affinity for CO_2 with a large binding energy (–3.627 eV), exceeding the performance of comparable MXenes and traditional catalysts. The strong adsorption is facilitated by charge transfer from scandium d-orbitals, resulting in effective activation of the CO_2 molecule, as confirmed by charge density difference and COHP analyses.

The Sc_2N surface also enables hydrogen dissociation and stabilizes key intermediates (e.g. COOH, HCOOH, CH_2OH), supporting a viable hydrogenation pathway to CH_4. Among the eight hydrogenation steps, $CH_2OH + H \rightarrow CH_3OH$ exhibits the highest activation energy (2.916 eV), marking it as the rate-determining step. Nevertheless, the overall pathway is thermodynamically downhill, suggesting that favourable kinetics could be obtained under appropriate conditions.

Sc_2N demonstrates strong potential for CO_2 capture and activation, with favourable adsorption energies and reaction energetics for intermediate hydrogenation steps along the

HCOOH pathway. However, the highly exothermic energy profile of the reaction pathway is primarily driven by the strong adsorption of atomic H and O species. This trend suggests a risk of surface poisoning due to the accumulation of these species at the surface, which could limit catalytic turnover under practical conditions. Therefore, while Sc_2N is promising for CO_2 capture, its catalytic viability may depend on strategies to regenerate active sites, such as co-catalyst design, applied bias or thermal treatment, to mitigate surface blocking and maintain continuous reactivity.

It is also important to note that all calculations were performed in the gas phase, neglecting solvent effects that could be present in an electrochemical environment. Solvent interactions may stabilize certain intermediates, modify adsorption energies and lower activation barriers through solvation and hydrogen bonding. The inclusion of solvent effects, either via implicit continuum models or explicit water layers, could thus provide deeper insight into the catalytic performance of Sc_2N MXenes.

In summary, Sc_2N MXenes combine strong CO_2 adsorption, intermediate stabilization and electronic tunability, making them attractive candidates for CO_2 capture and methane production within CCU technologies. While the current study provides robust theoretical support, future work should incorporate solvent effects and explore regeneration mechanisms to enhance the practical applicability of Sc_2N as a catalytic material.

Data accessibility. All data are contained within the manuscript and electronic supplementary material [76].

Declaration of AI use. We have not used AI-assisted technologies in creating this article.

Authors' contributions. M.P.: data curation, investigation, visualization, writing—original draft; S.S.T.: conceptualization, investigation, supervision, validation, writing—original draft; N.H.d.L.: formal analysis, resources, validation, writing—review and editing.

All authors gave final approval for publication and agreed to be held accountable for the work performed therein.

Conflict of interest declaration. We declare we have no competing interests.

Funding. We are grateful to the Research Affairs Division of the Amirkabir University of Technology (AUT), Tehran, Iran, for financial support. S.S.T. thanks the UK Royal Society for an International Exchanges grant (IES\R3\223184).

Acknowledgements. This research has utilized the ARCHER2 UK National Supercomputing Service (https://www.archer2.ac.uk) through our membership of the HEC Materials Chemistry Consortium funded by UK Engineering and Physical Sciences Research Council (EP/R029431). The computational resources of the Advanced Research Computing at Cardiff (ARCCA) Division, Cardiff University, and HPC Wales were also employed for this study.

References

1. Muntone S. 2013 *Education.com. The mcgraw-hill companies*. vol. **14**.
2. Ritchie H, Roser M. 2018 . *Our World in Data. See Https://Ourworldindata.Org/Plastic-Pollution*
3. Yoro KO, Daramola MO. 2020 *Advances in carbon capture*, pp. 3–28. Amsterdam, The Netherlands: Elsevier. (doi:10.1016/B978-0-12-819657-1.00001-3)
4. I. P. O. C. Change. 2007 . *Agenda* **6**, 333.
5. Ritchie H, Rosado P, Roser M. 2023 *Our world in data*. See https://ourworldindata.org/co2-and-greenhouse-gas-emissions.
6. Hansen J, Sato M, Ruedy R. 2012 . *Proc. Natl Acad. Sci. USA* **109**, E2415–E2423.
7. Solomon S, Plattner GK, Knutti R, Friedlingstein P. 2009 . *Proc. Natl Acad. Sci. USA* **106**, 1704–1709.
8. Upadhyay RK. 2020 . *Am. J. Clim. Chang.* **9**, 159.
9. Quéré CL *et al*. 2013 . *Earth Syst. Sci. Data* **5**, 165–185.
10. Houghton RA, Nassikas AA. 2017 . *Glob. Biogeochem. Cycles* **31**, 456–472.
11. I. C. Change. 2014 *Contribution of working group III to the fifth assessment report of the intergovernmental panel on climate change*, p. 147, vol. **1454**.
12. Amer-Wahlin I, Hellsten C, Noren H. 2006 . *Obstet. Gynecol.* **186**, 268–273.

13. Rubin ES, Davison JE, Herzog HJ. 2015 . *Int. J. Greenh. Gas Control* **40**, 378–400.
14. Metz B, Davidson O, Bosch P, Dave R, Meyer L. 2007 In *Contribution of Working Group II to the Fourth Assessment Report of the Intergovernmental Panel on Climate Change (IPCC)*.
15. Naguib M, Mochalin VN, Barsoum MW, Gogotsi Y. 2014 . *Adv. Mater.* **26**, 992–1005.
16. Naguib M, Kurtoglu M, Presser V, Lu J, Niu J, Heon M, Hultman L, Gogotsi Y, Barsoum MW. 2011 . *Adv. Mater.* **23**, 4248–4253.
17. Anasori B, Lukatskaya MR, Gogotsi Y. 2017 . *Nat. Rev. Mater.* **2**, 1–17.
18. Li B, Duan Y, Luebke D, Morreale B. 2013 . *Appl. Energy* **102**, 1439–1447.
19. Wang P, Wang B, Wang R. 2023 . *Materials* **16**, 6816.
20. Rahman UU, Humayun M, Ghani U, Usman M, Ullah H, Khan A, El-Metwaly NM, Khan A. 2022 . *Molecules* **27**, 4909.
21. Handoko AD, Khoo KH, Tan TL, Jin H, Seh ZW. 2018 . *J. Mater. Chem. A* **6**, 21885–21890. (doi:10.1039/C8TA06567E)
22. Meng L, Yan LK, Viñes F, Illas F. 2024 . *J. Mater. Chem. A* **12**, 7856–7874. (doi:10.1039/D4TA00320A)
23. Khanam R, Fozia S, Dar MA. 2024 . *Sustain. Energy Fuels* **8**, 5595–5607. (doi:10.1039/D4SE00582A)
24. Khazaei M, Arai M, Sasaki T, Chung CY, Venkataramanan NS, Estili M, Sakka Y, Kawazoe Y. 2013 . *Adv. Funct. Mater.* **23**, 2185–2192. (doi:10.1002/adfm.201202502)
25. Goel N, Kushwaha A, Kumar M. 2022 . *RSC Adv.* **12**, 25172–25193.
26. Mozafari M, Soroush M. 2021 . *Mater. Adv.* **2**, 7277–7307. (doi:10.1039/D1MA00625H)
27. Kumar S, Schwingenschlögl U. 2016 . *Phys. Rev. B* **94**, 035405. (doi:10.1103/PhysRevE.94.062404)
28. Balcı E, Akkuş ÜÖ, Berber S. 2018 . *J. Phys. Condens. Matter* **30**, 155501.
29. Chen Q, Zhang D, Pan J, Fan W. 2020 . *Optik* **219**, 165046. (doi:10.1016/j.ijleo.2020.165046)
30. López M, Morales-García Á, Viñes F, Illas F. 2021 . *ACS Catal.* **11**, 12850–12857. (doi:10.1021/acscatal.1c03150)
31. Jurado A, Ibarra K, Morales-García Á, Viñes F, Illas F. 2021 . *ChemPhysChem* **22**, 2456–2463.
32. Hohenberg P, Kohn W. 1964 . *Phys. Rev.* **136**, B864–B871. (doi:10.1103/PhysRev.136.B864)
33. Kohn W, Sham LJ. 1965 . *Phys. Rev.* **140**, A1133–A1138. (doi:10.1103/PhysRev.140.A1133)
34. Kresse G, Hafner J. 1993 Ab initio molecular dynamics for liquid metals. *Phys. Rev. B Condens. Matter* **47**, 558–561. (doi:10.1103/PhysRevB.47.558)
35. Kresse G, Furthmüller J. 1996 Efficient iterative schemes for ab initio total-energy calculations using a plane-wave basis set. *Phys. Rev. B Condens. Matter* **54**, 11169–11186. (doi:10.1103/PhysRevB.54.11169)
36. Kresse G, Hafner J. 1993 Ab initio molecular dynamics for open-shell transition metals. *Phys. Rev. B Condens. Matter* **48**, 13115–13118. (doi:10.1103/PhysRevB.48.13115)
37. Perdew JP, Burke K, Ernzerhof M. 1996 . *Phys. Rev. Lett.* **77**, 3865.
38. Perdew JP, Burke K, Ernzerhof M. 1998 . *Phys. Rev. Lett.* **80**, 891. (doi:10.1103/PhysRevLett.80.891)
39. Morales-Salvador R, Gouveia JD, Morales-García Á, Viñes F, Gomes JRB, Illas F. 2021 . *ACS Catal.* **11**, 11248–11255. (doi:10.1021/acscatal.1c02663)
40. Kresse G, Joubert D. 1999 . *Phys. Rev. B* **59**, 1758. (doi:10.1103/PhysRevB.59.1758)
41. Yu J, Xie LH, Li JR, Ma Y, Seminario JM, Balbuena PB. 2017 CO_2 capture and separations using MOFs: computational and experimental studies. *Chem. Rev.* **117**, 9674–9754. (doi:10.1021/acs.chemrev.6b00626)
42. Orhan IB, Le TC, Babarao R, Thornton AW. 2023 . *Commun. Chem.* **6**, 214.
43. Faraji M, Bafekry A, Fadlallah MM, Molaei F, Hieu NN, Qian P, Ghergherehchi M, Gogova D. 2021 Surface modification of titanium carbide MXene monolayers (Ti_2C and Ti_3C_2) via chalcogenide and halogenide atoms. *Phys. Chem. Chem. Phys.* **23**, 15319–15328. (doi:10.1039/D1CP01788H)
44. Monkhorst HJ, Pack JD. 1976 . *Phys. Rev. B* **13**, 5188. (doi:10.1103/PhysRevB.13.5188)
45. Grimme S, Ehrlich S, Goerigk L. 2011 . *J. Comput. Chem.* **32**, 1456–1465.
46. Tafreshi SS, Ranjbar M, Taghizade N, Panahi S, Jamaati M, Leeuw NH. 2022 . *ChemPhysChem* **23**, 202100781.
47. Tafreshi SS, Panahi S, Taghizade N, Jamaati M, Ranjbar M, Leeuw NH. 2022 . *Catalysts* **12**, 1275. (doi:10.3390/catal12101275)

48. Thirumuruganandham SP, Figueroa JLC, Baños AT, Mowbray DJ, Terencio T, Martinez MO. 2022 Ab initio calculations of chitosan effects on the electronic properties of unpassivated triangular ZnO nanowires oriented along [0001] directions. *ACS Omega* **8**, 2337–2343. (doi:10.1021/acsomega.2c06740)
49. Mills G, Jónsson H, Schenter GK. 1995 . *Surf. Sci.* **324**, 305–337. (doi:10.1016/0039-6028(94)00731-4)
50. Jónsson H, Mills G, Jacobsen KW. 1998 *Classical and quantum dynamics in condensed phase simulations*, pp. 385–404. Singapore: World Scientific. (doi:10.1142/9789812839664_0016)
51. Hess F, Smarsly BM, Over H. 2020 . *Acc. Chem. Res.* **53**, 380–389.
52. Bhat A, Anwer S, Bhat KS, Mohideen MIH, Liao K, Qurashi A. 2021 . *Npj 2D Mater. Appl.* **5**, 61.
53. Wang Y, He D, Chen H, Wang D. 2019 . *J. Photochem. Photobiol. C Photochem. Rev.* **40**, 117–149.
54. Kunkel C, Viñes F, Illas F. 2016 . *Energy Environ. Sci.* **9**, 141–144. (doi:10.1039/C5EE03649F)
55. Matsuda S, Mukai T, Sakurada S, Uchida N, Umeda M. 2019 . *New J. Chem.* **43**, 13717–13720. (doi:10.1039/C9NJ03092A)
56. Liu X, Yao L, Zhang S, Huang C, Yang W. 2024 Theoretical study of electrocatalytic CO_2 reduction mechanism on typical MXenes under realistic conditions. *Inorg. Chem.* **63**, 6305–6314. (doi:10.1021/acs.inorgchem.4c00072)
57. Wang B, Zhou A, Liu F, Cao J, Wang L, Hu Q. 2018 . *J. Adv. Ceram.* **7**, 237–245. (doi:10.1007/s40145-018-0275-3)
58. Henkelman G, Arnaldsson A, Jónsson H. 2006 . *Comput. Mater. Sci.* **36**, 354–360. (doi:10.1016/j.commatsci.2005.04.010)
59. Khanam R, Hassan A, Nazir Z, Dar MA. 2023 . *Sustain. Energy Fuels* **7**, 5046–5056. (doi:10.1039/D3SE00830D)
60. Fozia S, Hassan A, Reshi SA, Singh P, Bhat GA, Dixit M, Dar MA. 2023 . *J. Phys. Chem. C* **127**, 11911–11920. (doi:10.1021/acs.jpcc.3c00387)
61. Dronskowski R, Bloechl PE. 1993 . *J. Phys. Chem.* **97**, 8617–8624. (doi:10.1021/j100135a014)
62. Deringer VL, Tchougréeff AL, Dronskowski R. 2011 . *J. Phys. Chem. A* **115**, 5461–5466.
63. Maintz S, Deringer VL, Tchougréeff AL, Dronskowski R. 2013 . *J. Comput. Chem.* **34**, 2557–2567.
64. Maintz S, Deringer VL, Tchougréeff AL, Dronskowski R. 2016 . *J. Comput. Chem.* **37**, 1030–1035.
65. Morales-Salvador R, Morales-García Á, Vines F, Illas F. 2018 Two-dimensional nitrides as highly efficient potential candidates for CO_2 capture and activation. *Phys. Chem. Chem. Phys.* **20**, 17117–17124. (doi:10.1039/C8CP02746C)
66. Scaranto J, Mavrikakis M. 2016 . *Surf. Sci.* **648**, 201–211. (doi:10.1016/j.susc.2015.09.023)
67. Gautier S, Steinmann SN, Michel C, Fleurat-Lessard P, Sautet P. 2015 . *Phys. Chem. Chem. Phys.* **17**, 28921–28930.
68. Atrak N, Tayyebi E, Skúlason E. 2023 . *Catal. Sci. Technol.* **13**, 3321–3336. (doi:10.1039/D2CY02175G)
69. Gao W, Chen Y, Li B, Liu SP, Liu X, Jiang Q. 2020 Determining the adsorption energies of small molecules with the intrinsic properties of adsorbates and substrates. *Nat. Commun.* **11**, 1196. (doi:10.1038/s41467-020-14969-8)
70. Abraham BM, Piqué O, Khan MA, Viñes F, Illas F, Singh JK. 2023 Machine learning-driven discovery of key descriptors for CO_2 activation over two-dimensional transition metal carbides and nitrides. *ACS Appl. Mater. Interfaces* **15**, 30117–30126. (doi:10.1021/acsami.3c02821)
71. Li J, Wang Z, Chen H, Zhang Q, Hu H, Liu L, Ye J, Wang D. 2021 . *Catal. Sci. Technol.* **11**, 4953–4961. (doi:10.1039/D1CY00716E)
72. Amrillah T, Supandi AR, Puspasari V, Hermawan A, Seh ZW. 2022 . *Trans. Tianjin Univ.* **28**, 307–322. (doi:10.1007/s12209-022-00328-9)
73. Hou T *et al*. 2020 . *Nat. Commun.* **11**, 4251.
74. Kabir L, Wijaya K, Oh WC. 2024 . *Sustain. Energy Fuels* **8**, 2535–2569. (doi:10.1039/D4SE00405A)
75. Tafreshi SS, Ranjbar M, Jamaati M, Panahi S, Taghizade N, Torkashvand M, Leeuw NH. 2023 . *Phys. Chem. Chem. Phys.* **25**, 2498–2509. (doi:10.1039/D2CP04749G)

76. De Leeuw NH, Sarabadani Tafreshi S, Parto M. 2026 Supplementary material from: Two-dimensional Sc2N MXenes as efficient solid catalysts for CO_2 adsorption and conversion: a density functional theory study. Figshare. (doi:10.6084/m9.figshare.c.8331837)